Article

Nanosheet-Like Ho_2O_3 and Sr-Ho_2O_3 Catalysts for Oxidative Coupling of Methane

Yuqiao Fan [1], Changxi Miao [2,*], Yinghong Yue [1], Weiming Hua [1,*] and Zi Gao [1]

[1] Shanghai Key Laboratory of Molecular Catalysis and Innovative Materials, Department of Chemistry, Fudan University, Shanghai 200438, China; 18110220090@fudan.edu.cn (Y.F.); yhyue@fudan.edu.cn (Y.Y.); zigao@fudan.edu.cn (Z.G.)

[2] Shanghai Research Institute of Petrochemical Technology SINOPEC, Shanghai 201208, China

[*] Correspondence: miaocx.sshy@sinopec.com (C.M.); wmhua@fudan.edu.cn (W.H.); Tel.: +86-21-31249121 (W.H.)

Abstract: In this work, Ho_2O_3 nanosheets were synthesized by a hydrothermal method. A series of Sr-modified Ho_2O_3 nanosheets (Sr-Ho_2O_3-NS) with a Sr/Ho molar ratio between 0.02 and 0.06 were prepared via an impregnation method. These catalysts were characterized by several techniques such as XRD, N_2 adsorption, SEM, TEM, XPS, O_2-TPD (temperature-programmed desorption), and CO_2-TPD, and they were studied with respect to their performances in the oxidative coupling of methane (OCM). In contrast to Ho_2O_3 nanoparticles, Ho_2O_3 nanosheets display greater CH_4 conversion and C_2-C_3 selectivity, which could be related to the preferentially exposed (222) facet on the surface of the latter catalyst. The incorporation of small amounts of Sr into Ho_2O_3 nanosheets leads to a higher ratio of $(O^- + O_2^-)/O^{2-}$ as well as an enhanced amount of chemisorbed oxygen species and moderate basic sites, which in turn improves the OCM performance. The optimal catalytic behavior is achievable on the 0.04Sr-Ho_2O_3-NS catalyst with a Sr/Ho molar ratio of 0.04, which gives a 24.0% conversion of CH_4 with 56.7% selectivity to C_2-C_3 at 650 °C. The C_2-C_3 yield is well correlated with the amount of moderate basic sites present on the catalysts.

Keywords: oxidative coupling of methane; Ho_2O_3-based nanosheets; morphology effect; Sr modification

1. Introduction

The present energy crisis, owing to the dwindling petroleum resource and its nonrenewable feature, must be solved as soon as possible. Methane, as a major component of natural gas, coal-bed gas, and shale gas, is attracting increasing attention as a clean fossil energy and a raw material for producing chemicals. Methane conversion can proceed via nondirect and direct routes [1–7]. The oxidative coupling of methane (OCM) to ethylene and ethane (C_2 hydrocarbons) is an indispensable way that has great prospect in the direct conversion of methane into value-added products [5–7]. Ethylene is one of the most important parts in petrochemical fields. Ethylene and its derivatives are associated closely with over 70% of petroleum chemicals. Since 1982 Keller et al. [8] first reported the OCM technology, it has attracted more and more attention in catalysis, chemical industry, and oil and gas fields because of its potential economic value and application prospect.

Up to now, several types of catalysts have been tried for OCM reaction [5,7]. It is widely accepted that Li/MgO and Mn-Na_2WO_4/SiO_2 are the most promising catalysts for application, and they have been widely researched [9–23]. In general, higher reaction temperatures (above 800 °C) are required for both kinds of catalysts to achieve the optimal OCM performance. Wang et al. [24] reduced the reaction temperature from 800 to 720 °C by doping Ti into Mn-Na_2WO_4/SiO_2, and they acquired 26% CH_4 conversion with 76% C_2-C_3 selectivity. More studies are now shifted to a low-temperature OCM process. Nanoscale rare earth oxide-based catalysts with special morphologies (nanorods and nanosheets),

such as CeO_2, La_2O_3, Sm_2O_3, and Er_2O_3, were found to effectively catalyze the OCM process at lower temperatures (500–650 °C) [25–30]. However, the C_2 selectivity and yield still need to improve.

Ho_2O_3 was demonstrated to have potential application for high-*k* dielectric material [31], photocatalysts [32,33], and energy-storage electrodes [34]. There are few reports dealing with the use of Ho_2O_3 as a catalyst in the OCM process [35]. In this work, we synthesized Ho_2O_3 and Sr-Ho_2O_3 nanosheets to develop a new type of efficient catalyst system for a low-temperature OCM reaction. The catalytic performances of these catalysts were related to their characterization results.

2. Results and Discussion
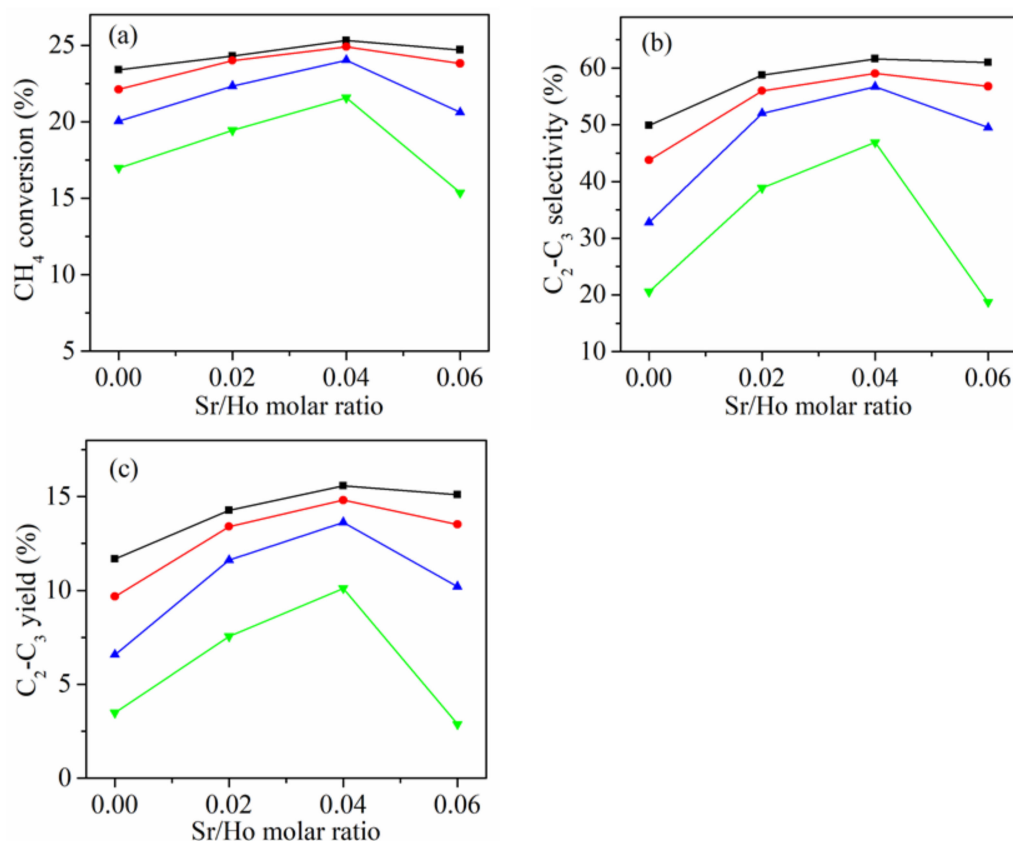
2.1. Catalytic Performances

We first compared catalytic behaviors of Ho_2O_3 nanosheets and nanoparticles for the OCM reaction to investigate the morphology effect of the Ho_2O_3 catalysts. As shown in Figure 1, with the reaction temperature raised from 600 to 750 °C, the CH_4 conversion increases progressively, while the selectivity to C_2-C_3 (C_2H_4, C_2H_6, C_3H_6, and C_3H_8) rises more evidently. Because of this, the C_2-C_3 yield also improves with the temperature. It is evident that the OCM performance is better over Ho_2O_3-NS nanosheets than Ho_2O_3-NP nanoparticles. For instance, the CH_4 conversion, C_2-C_3 selectivity, and yield over Ho_2O_3-NS at 700 °C are 22.1%, 43.8%, and 9.7%, respectively, and those over Ho_2O_3-NP are 17.8%, 29.7%, and 5.3%, respectively. The shape effects of La_2O_3, Sm_2O_3, and Er_2O_3 catalysts on the OCM reaction were also reported by Zhu et al. and in our recent work [25–28].
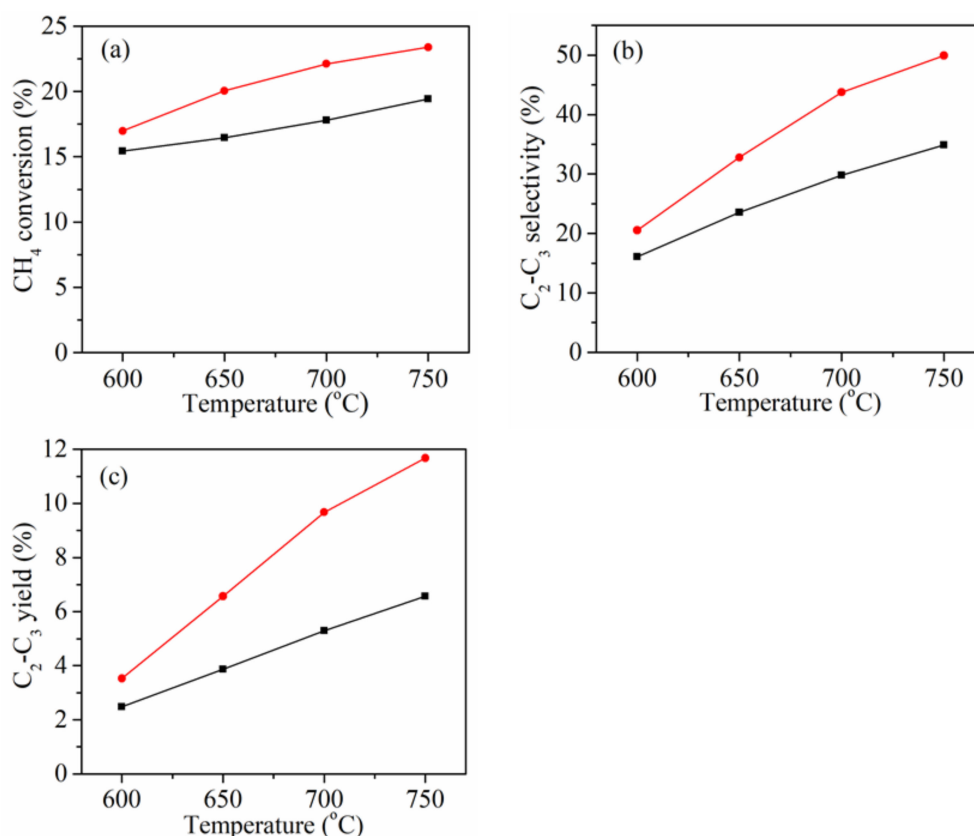
Figure 1. CH_4 conversion (**a**), C_2-C_3 selectivity (**b**) and C_2-C_3 yield (**c**) as a function of reaction temperature for the Ho_2O_3 catalysts. (■) Ho_2O_3-NP (nanoparticles), (●) Ho_2O_3-NS (nanosheet).

We then tested the catalytic performances of Sr-modified Ho_2O_3 nanosheets (Sr-Ho_2O_3-NS) to investigate the impact of Sr modification on Ho_2O_3-NS nanosheets in the OCM reaction. As the Sr/Ho molar ratio is increased from 0 to 0.06, the CH_4 conversion, C_2-C_3

selectivity, and the yield first rise and then diminish (Figure 2). The 0.04Sr-Ho$_2$O$_3$-NS catalyst with a Sr/Ho ratio of 0.04 exhibits the best OCM performance. This catalyst yields a 24.0% CH$_4$ conversion and 56.7% C$_2$-C$_3$ selectivity at 650 °C. Even at a low temperature of 600 °C, a 21.6% CH$_4$ conversion and 46.9% C$_2$-C$_3$ selectivity can be achieved. Notably, the 0.04Sr-Ho$_2$O$_3$-NS catalyst performs better than Ho$_2$O$_3$-NS (20.0% CH$_4$ conversion and 32.8% C$_2$-C$_3$ selectivity at 650 °C). The typical product distribution over the Ho$_2$O$_3$-NS and Sr-Ho$_2$O$_3$-NS catalysts at 650 °C is listed in Table 1. According to the literature [5,36,37], the proposed reaction mechanism of methane transformation to ethane and ethylene is shown in Scheme S1. The interaction of the adsorbed CH$_4$ and O$_2$ generates methyl radicals (CH$_3$). The coupling of CH$_3$ radicals generates C$_2$H$_6$, followed by the dehydrogenation to C$_2$H$_4$. Propane and propylene can be formed in the similar way, as illustrated in Scheme S1. The results shown in Figure 2 indicate that the introduction of appropriate amounts of Sr to Ho$_2$O$_3$-NS is beneficial for the OCM reaction. It is noteworthy that the 0.06Sr-Ho$_2$O$_3$-NS catalyst shows a bit lower CH$_4$ conversion and C$_2$-C$_3$ selectivity than 0.04Sr-Ho$_2$O$_3$-NS at 750 °C and 700 °C, which could be attributed to the blockage of some active sites upon introducing excessive Sr. However, much worse OCM performance was observed for the former catalyst than the latter one at 650 °C and 600 °C, particularly at 600 °C. It was also reported that there were the optimal contents of Na and Li for Na-CaO and for the Li-promoted Bi-Mn oxide catalysts employed in the OCM reaction [38,39].


Figure 2. Effect of Sr/Ho molar ratio on catalytic performances of Sr-modified Ho$_2$O$_3$ nanosheet (Sr-Ho$_2$O$_3$-NS) catalysts at different temperatures: (**a**) CH$_4$ conversion, (**b**) C$_2$-C$_3$ selectivity, and (**c**) C$_2$-C$_3$ yield. (▼) 600 °C, (▲) 650 °C, (●) 700 °C, (■) 750 °C.

Table 1. Reaction data of the Ho_2O_3-NS and Sr-Ho_2O_3-NS catalysts at 650 °C.

| Catalyst | Conversion of CH_4 (%) | Selectivity (%) | | | | | | Selectivity of C_2-C_3 (%) | Yield of C_2-C_3 (%) |
		C_2H_4	C_2H_6	C_3H_6	C_3H_8	CO_2	CO		
Ho_2O_3-NS	20.0	14.9	17.1	0.3	0.5	40.4	26.8	32.8	6.6
0.02Sr-Ho_2O_3-NS	22.3	25.5	23.5	1.5	1.5	36.1	11.9	52.0	11.6
0.04Sr-Ho_2O_3-NS	24.0	27.4	26.0	1.6	1.7	35.5	7.8	56.7	13.6
0.06Sr-Ho_2O_3-NS	20.6	21.9	24.9	1.2	1.5	38.9	11.6	49.5	10.2

We selected the best 0.04Sr-Ho_2O_3-NS catalyst to investigate the lifetime for the OCM reaction, which was evaluated at 650 °C. It is clear from the results presented in Figure 3 that the 0.04Sr-Ho_2O_3-NS catalyst shows good stability during 60 h of the reaction, maintaining ca. 24% CH_4 conversion with 57% C_2-C_3 selectivity.
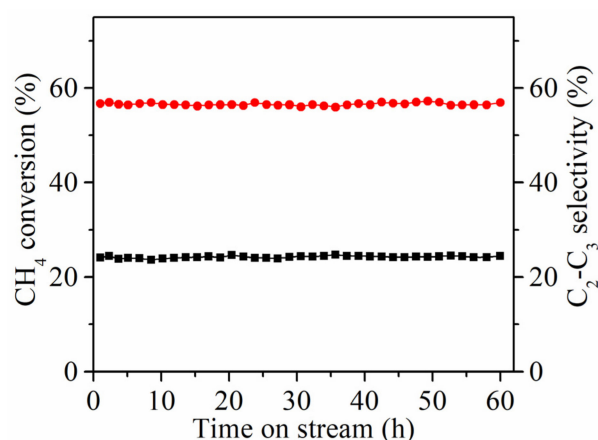
Figure 3. CH_4 conversion (■) and C_2-C_3 selectivity (●) with time on stream over 0.04Sr-Ho_2O_3-NS at 650 °C.

We compared the catalytic performances of our catalyst 0.04Sr-Ho_2O_3-NS and three reference catalysts, i.e., 0.04Sr-La_2O_3 nanofibers, 0.04Sr-CeO_2 nanowires, and 3% Li/MgO. As shown in Figure S1, both 0.04Sr-CeO_2 and 3% Li/MgO are inactive at 600 and 650 °C. Our catalyst 0.04Sr-Ho_2O_3 displays a higher methane conversion and C_2-C_3 selectivity than the three reference catalysts at 600–750 °C.

2.2. Structural and Textural Properties

Figure 4 presents the XRD patterns of the Ho_2O_3 nanoparticles and nanosheets, as well as the Sr-modified Ho_2O_3 nanosheets. These samples display similar characteristics of diffraction peaks that belong to the cubic Ho_2O_3 phase (PDF #43-1018). The diffraction peaks at about 21°, 29°, 34°, 36°, 40°, 44°, 49°, 53°, 56°, 58°, 59°, and 60° correspond to the (211), (222), (400), (411), (332), (134), (440), (611), (145), (622), (136), and (444) planes of the cubic phase of Ho_2O_3, respectively. The absence of any other crystal phases on the XRD profiles is a consequence of having lower contents of Sr and high dispersion of Sr in the catalysts. Table 2 shows that in comparison with Ho_2O_3-NS, the Sr-modified Ho_2O_3 nanosheets display greater lattice parameters (1.0571–1.0589 nm vs. 1.0561 nm). This observation implies that Sr is doped into the lattice of Ho_2O_3, considering that Sr^{2+} has larger ionic radius than Ho^{3+} (0.118 nm vs. 0.090 nm). The doping of Sr into the lattice of La_2O_3 via an impregnation method, followed by calcination at high temperatures, was also displayed in former studies [29,40].
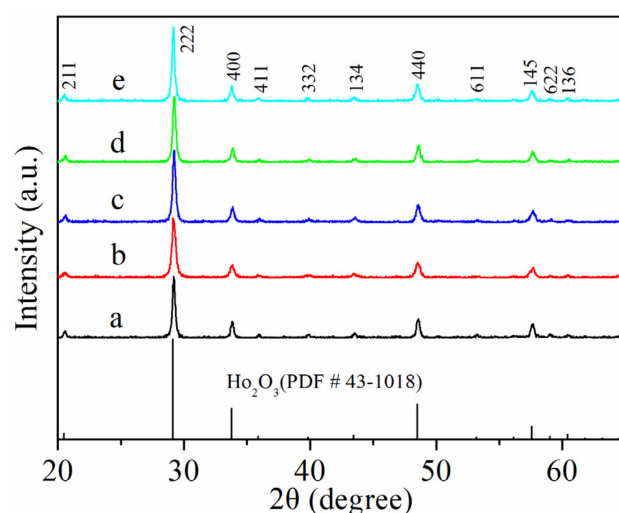
Figure 4. XRD patterns of the catalysts. (a) Ho_2O_3-NP, (b) Ho_2O_3-NS, (c) 0.02Sr-Ho_2O_3-NS, (d) 0.04Sr-Ho_2O_3-NS, (e) 0.06Sr-Ho_2O_3-NS.

Table 2. Textural properties and XPS data of the Ho_2O_3-based catalysts.

Catalyst	S_{BET} (m²/g)	Average size (nm)	$a = b = c$ (nm)[d]	O 1s BE[e], FWHM[f] (eV)				$(O^- + O_2^-)/O^{2-}$
				O^{2-}	O^-	CO_3^{2-}	O_2^-	
Ho_2O_3-NP	7.9	17.5 ± 3.3	1.0560	529.3/1.7	530.8/1.7	531.8/1.2	532.7/1.2	1.4
Ho_2O_3-NS	6.1	771 ± 232 [a] 81.9 ± 21.0 [b]	1.0561	529.3/1.6	530.6/1.5	531.6/1.1	532.5/1.4	1.7
0.02Sr-Ho_2O_3-NS	7.5	— [c]	1.0571	529.3/1.5	530.8/1.7	531.8/1.2	532.6/1.4	1.9
0.04Sr-Ho_2O_3-NS	7.7	761 ± 184 [a] 82.5 ± 27.9 [b]	1.0580	529.6/1.5	530.9/1.6	532.0/1.4	532.8/1.3	2.2
0.06Sr-Ho_2O_3-NS	7.2	— [c]	1.0589	529.2/1.8	530.7/1.5	531.6/1.2	532.5/1.3	2.0

[a] Average width of nanosheets; [b] Average thickness of nanosheets; [c] Not measured; [d] Lattice parameter; [e] Binding energy; [f] Full width at half maximum.

The SEM images of Ho_2O_3-NS and 0.04Sr-Ho_2O_3-NS are shown in Figure 5. Clearly, both catalysts display a nanosheet morphology. The morphology of nanoparticles with an irregular shape can be found for Ho_2O_3-NP (Figure S2). The average width and thickness of Ho_2O_3-NS are 771 nm and 81.9 nm, respectively. Ho_2O_3-NP has a mean size of 17.5 nm. In addition, 0.04Sr-Ho_2O_3-NS has a similar size to Ho_2O_3-NS (Table 2), suggesting that the introduction of a small amount of Sr to Ho_2O_3-NS has a little impact on the catalyst size. As illustrated in Figure 6, the exposed facets of Ho_2O_3-NS and 0.04Sr-Ho_2O_3-NS can be clearly identified. The crystal lattice fringes marked on their surfaces are indexed to the (440) and (04$\bar{4}$) reflections of cubic Ho_2O_3. The Fourier transform patterns (insets) achieved from selected areas of the corresponding crystals suggest that they are sitting against a plane perpendicular to the [222] zone axis, demonstrating that the (222) facets are exposed on the surfaces of Ho_2O_3-NS and 0.04Sr-Ho_2O_3-NS.

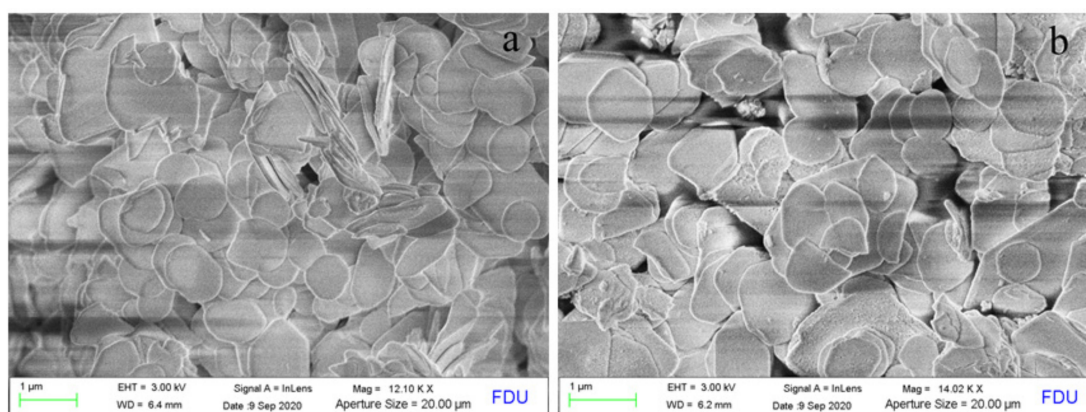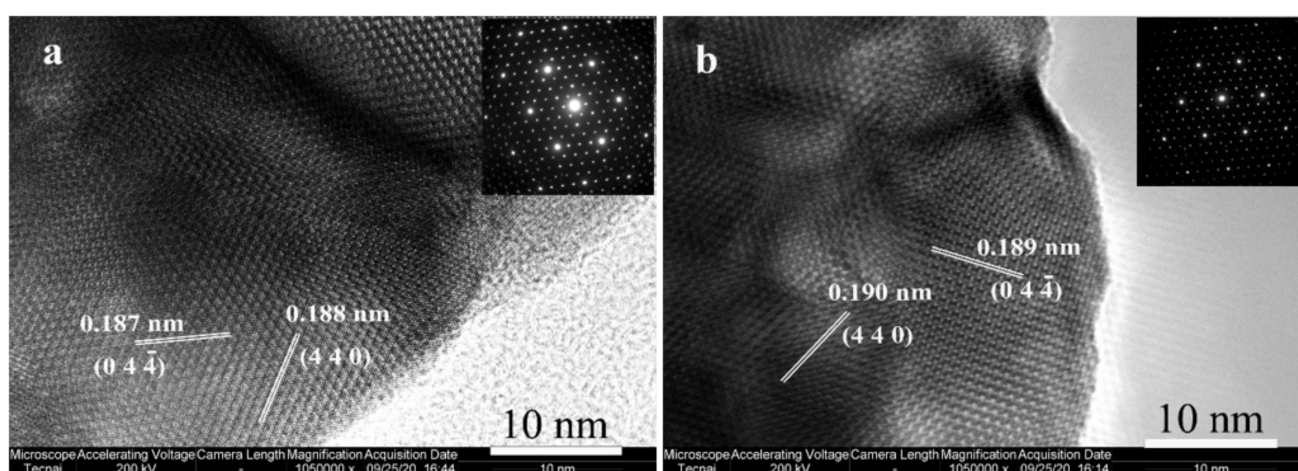**Figure 5.** SEM images of Ho_2O_3-NS (**a**) and 0.04Sr-Ho_2O_3-NS (**b**).

Figure 6. High resolution (HR) TEM graphs of Ho_2O_3-NS (**a**) and 0.04Sr-Ho_2O_3-NS (**b**). Insets are the fast Fourier transfer (FFT) patterns of the HR-TEM images.

The Brunauer–Emmett–Teller (BET) specific surface areas of the Ho_2O_3-based catalysts are given in Table 2. All catalysts give low surface areas between 6.1 and 7.9 m^2/g, which is preferred for the OCM reaction. In contrast to Ho_2O_3-NP, Ho_2O_3-NS has a lower surface area (6.1 vs. 7.9 m^2/g). The incorporation of small amounts of Sr into Ho_2O_3-NS slightly increases the surface area.

2.3. XPS and IR

Figure S3 shows the XPS spectra of O1s on Ho_2O_3-NP, Ho_2O_3-NS, and Sr-Ho_2O_3-NS catalysts. The XPS spectra were deconvoluted into four peaks corresponding to four different oxygen species. The XPS data are listed in Table 2. Oxygen species located at ~529.3, ~530.7, ~531.8, and ~532.6 eV are O^{2-} (lattice oxygen), O^- (peroxide ions), CO_3^{2-} (carbonate), and O_2^- (superoxide ions), respectively [25,41–44]. It is generally accepted that the surface electrophilic oxygen species O^- and O_2^- are beneficial for C_2 selectivity in the OCM reaction, while the lattice oxygen O^{2-} is responsible for the deep oxidation of CH_4 in forming CO and CO_2 [25,26,29,43,45]. The Ho_2O_3-NS catalyst gives a $(O^- + O_2^-)/O^{2-}$ ratio of 1.7, higher than Ho_2O_3-NP (1.4). The Sr-Ho_2O_3-NS catalysts have a higher ratio of $(O^- + O_2^-)/O^{2-}$ than Ho_2O_3-NS, and 0.04Sr-Ho_2O_3-NS possesses the highest $(O^- + O_2^-)/O^{2-}$ ratio (2.2). It is thus concluded that the Ho_2O_3-based catalysts with a higher $(O^- + O_2^-)/O^{2-}$ ratio display higher C_2 selectivity in the OCM reaction at 700 °C and 750 °C (Figures 1 and 2). This observation is in accord with the results reported for the OCM reaction catalyzed by the La_2O_3-based catalysts [26,29,40,45].

Based on theoretical studies, Sayle and co-workers have disclosed that the energy required to generate oxygen vacancies over CeO_2 for different crystal planes follows the order of (110) < (310) < (111) [46]. In other words, oxygen vacancies are easier to form on the (110) plane of CeO_2. The interaction between O_2 and oxygen vacancies generates the surface electrophilic oxygen species such as O^- and O_2^-. Therefore, we think that the higher $(O^- + O_2^-)/O^{2-}$ ratio observed over Ho_2O_3-NS than Ho_2O_3-NP could be associated with the predominantly exposed (222) planes over the former catalyst. It was found that the OCM process was a structure-sensitive reaction [25,30,44].

Figure 7 compares the FTIR spectra of 0.04Sr-Ho_2O_3-NS and 0.06Sr-Ho_2O_3-NS catalysts after the OCM reaction at 600 °C for 1 h. Two bands that appeared at 1637 and 3445 cm^{-1} are assigned to the bending and stretching vibrations of the O−H groups in H_2O [47]. The bands appearing at 858 and 1442 cm^{-1} correspond to the bending and asymmetric stretching vibrations of C−O in CO_3^{2-} [48,49], and they stemmed from the combination of catalysts with CO_2 produced during the OCM reaction. Clearly, the spent 0.06Sr-Ho_2O_3-NS catalyst displays a stronger intensity of CO_3^{2-} vibrations than the spent 0.04Sr-Ho_2O_3-NS, suggesting that the amount of carbonate is higher over the former catalyst than the latter one. Thus, the worse OCM performance observed for the former catalyst than the latter one at 650 °C and 600 °C (Figure 2) is due to the blockage of active sites by carbonate.
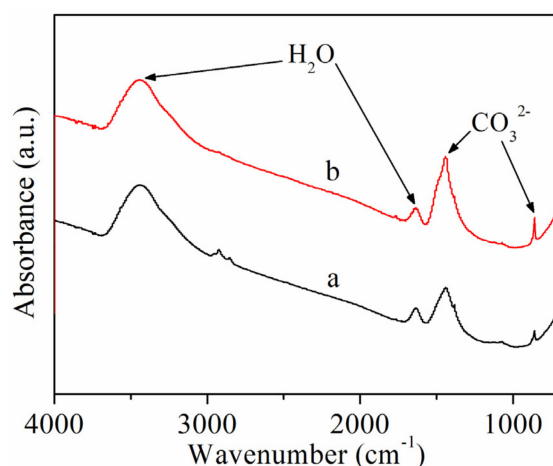

Figure 7. FTIR spectra of 0.04Sr-Ho_2O_3-NS (a) and 0.06Sr-Ho_2O_3-NS (b) catalysts after the oxidative coupling of methane (OCM) reaction at 600 °C for 1 h.

2.4. Temperature-Programmed Desorption (TPD) of O_2 and CO_2

To further understand the activation of oxygen over the catalysts, which plays an important role in the OCM process, the TPD of O_2 was performed. Figure 8 shows that there are two desorption peaks of oxygen from the surfaces of catalysts. The low-temperature peaks located at 85–137 °C are assigned to the desorption of molecular oxygen species (i.e., loosely bounded surface oxygen), and the high-temperature peaks located at 263–426 °C are ascribed to the desorption of chemisorbed oxygen species, which could be O^-, O_2^-, and O^{2-} [40,44,50] that stemmed from the interaction of O_2 with the Ho_2O_3-based catalysts. It is generally believed that the chemisorbed oxygen species benefit CH_4 activation and C_2 selectivity in the OCM process [25,44,50,51]. Table 3 shows that a greater number of chemisorbed oxygen species are achieved over Ho_2O_3-NS than Ho_2O_3-NP (15.9 vs. 12.8 μmol/g), which is responsible for the higher CH_4 conversion and the C_2-C_3 yield observed for the former catalyst than the latter one. The incorporation of small amounts of Sr into Ho_2O_3-NS leads to an increase in the quantity of chemisorbed oxygen species (19.8–24.2 μmol/g), indicative of enhancing the oxygen activation. The largest quantity of chemisorbed oxygen species are achieved over 0.04Sr-Ho_2O_3-NS. Moreover, introducing Sr into Ho_2O_3-NS weakens the interaction between oxygen and the Sr-Ho_2O_3-NS catalysts,

since the desorption peaks of chemisorbed oxygen species shift to low temperatures (from 344 °C to 263–309 °C). The doping of low-valence Sr into high-valence Ho_2O_3 can increase the quantity of oxygen vacancies [51–53], which promotes the activation toward oxygen, thus leading to an increased amount of chemisorbed oxygen species. As a result, the Sr-Ho_2O_3-NS catalysts exhibit better OCM performances than Ho_2O_3-NS. The optimal CH_4 conversion and C_2-C_3 yield are obtained on the 0.04Sr-Ho_2O_3-NS catalyst with a Sr/Ho molar ratio of 0.04.
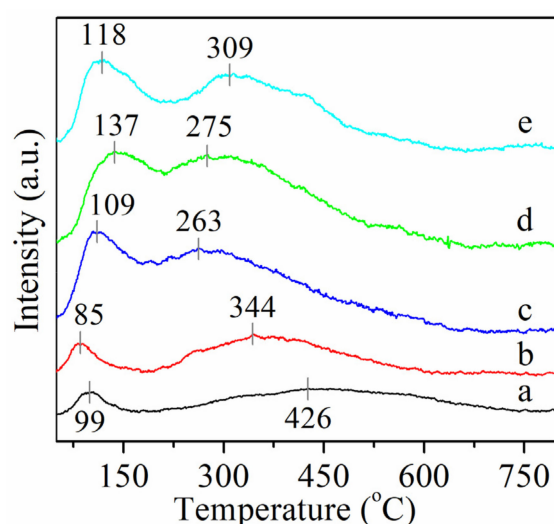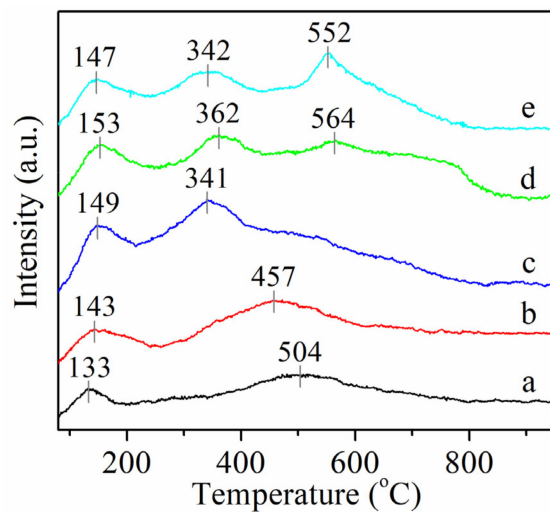

Figure 8. O_2-TPD (temperature programmed desorption) profiles of the catalysts. (a) Ho_2O_3-NP, (b) Ho_2O_3-NS, (c) 0.02Sr-Ho_2O_3-NS, (d) 0.04Sr-Ho_2O_3-NS, (e) 0.06Sr-Ho_2O_3-NS.

Table 3. O_2-TPD and CO_2-TPD data of the Ho_2O_3-based catalysts.

Catalyst	Peak Temperature (°C)		Amount of Desorbed O_2 (µmol/g)		Amount of Basic Sites (µmol/g)		
	I	II	I	II	Weak	Moderate	Total
Ho_2O_3-NP	99	426	2.3	12.8	3.2	16.3	19.5
Ho_2O_3-NS	85	344	2.2	15.9	7.0	30.1	37.1
0.02Sr-Ho_2O_3-NS	109	263	9.2	19.8	16.7	61.8	78.5
0.04Sr-Ho_2O_3-NS	137	275	11.3	24.2	16.2	69.9	86.1
0.06Sr-Ho_2O_3-NS	118	309	9.9	20.7	14.6	63.0	77.6

In addition to oxygen activation, the basicity of the catalysts is a key factor influencing the OCM reaction [54,55]. The surface basicity of the Ho_2O_3-NP, Ho_2O_3-NS, and Sr-Ho_2O_3-NS catalysts was measured by CO_2-TPD, and the results are presented in Figure 9 and Table 3. Figure 9 shows that there are two desorption peaks of CO_2 from the surfaces of the Ho_2O_3-NP, Ho_2O_3-NS, and 0.02Sr-Ho_2O_3-NS catalysts, while there are three CO_2 desorption peaks for the 0.04Sr-Ho_2O_3-NS and 0.06Sr-Ho_2O_3-NS catalysts. It was reported that the surface basic sites were associated closely with the O^-, O_2^- and O^{2-} oxygen species [10,51,54,56]. Based on the peak temperature of CO_2 desorption, the peaks that are below 200 °C, between 200 and 600 °C, and higher than 600 °C correspond to basic sites with weak, moderate, and strong strength, respectively [29,40,51]. Table 3 shows that the surfaces of all catalysts are dominated by moderate basic sites. Ho_2O_3-NS has a greater number of weak and moderate basic sites than Ho_2O_3-NP. The modification of Ho_2O_3-NS with Sr brings about an increase in the number of weak and moderate basic sites, and the number of moderate basic sites is increased to the maximum on 0.04Sr-Ho_2O_3-NS. As evidenced in Figure 10, the C_2-C_3 yield obtained at 700 °C correlates well with the number of moderate basic sites present on the Ho_2O_3-based catalysts. This finding is in accordance

with some previous reports that the surface basic sites with moderate strength are more favorable for the C_2 product formation in the OCM process [25,26,44,55,57–60].

Figure 9. CO_2-TPD profiles of the catalysts. (a) Ho_2O_3-NP, (b) Ho_2O_3-NS, (c) 0.02Sr-Ho_2O_3-NS, (d) 0.04Sr-Ho_2O_3-NS, (e) 0.06Sr-Ho_2O_3-NS.
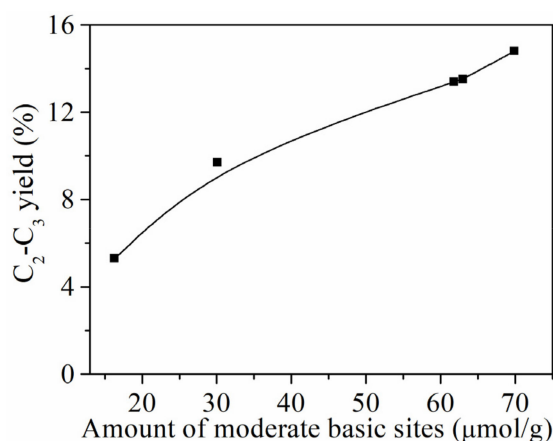
Figure 10. Relationship between the C_2-C_3 yield obtained at 700 °C and the amount of moderate basic sites present on the Ho_2O_3-based catalysts.

3. Materials and Methods

3.1. Catalyst Preparation

Ho_2O_3 nanosheets (labelled as Ho_2O_3-NS) were synthesized by a hydrothermal method reported by Lee and co-workers [61]. Typically, 3.79 g of $HoCl_3\bullet6H_2O$ was dissolved in 100 mL deionized water, and 1 mL of aqueous ammonia (25–28 wt%) was then added dropwise to the above solution under stirring. The obtained suspension was transferred into a Teflon-lined stainless autoclave, which was placed in an oven setting at 200 °C for 12 h. Ho_2O_3 nanoparticles (named as Ho_2O_3-NP) were prepared via a conventional precipitate method; 3.0 mL of aqueous ammonia (25–28 wt%) was added dropwise to 100 mL of 0.1 M $HoCl_3$ solution under stirring. All the resulting precipitates were fully washed with deionized water, followed by drying at 80 °C in an oven for 12 h. Finally, the dried $Ho(OH)_3$ samples were calcined at 750 °C in air for 4 h in a muffle to obtain Ho_2O_3 nanosheets and nanoparticles.

Sr-modified Ho_2O_3 nanosheets were synthesized by an incipient wetness impregnation method. In a typical procedure, different amounts of $Sr(NO_3)_2$ were dissolved in deionized water, and then a certain amount of dried $Ho(OH)_3$ nanosheets were added.

After drying under an infrared lamp, the sample was dried at 80 °C in an oven for 12 h, followed by calcination at 750 °C in air for 4 h in a muffle. The resulting catalysts were labelled as xSr-Ho$_2$O$_3$-NS, where x represents the Sr/Ho molar ratio (x = 0.02, 0.04, and 0.06, respectively).

For comparison, 0.04Sr-La$_2$O$_3$ nanofibers were prepared according to the literature [29]. Ce(OH)$_3$ nanowires were prepared according to the literature [30]. The 0.04Sr-CeO$_2$ nanowires were prepared in the same way as our Sr-modified Ho$_2$O$_3$ nanosheets. The 3% Li/MgO was prepared according to the literature [62]. The calcination temperature for three reference catalysts was 750 °C. The Sr/La or Sr/Ce molar ratio was 0.04. The content of Li in the catalyst was 3 wt.%.

3.2. Characterization of the Catalyst

X-ray diffraction (XRD) patterns were recorded on a D2 PHASER X-ray diffractometer using nickel-filtered Cu Kα radiation at 30 kV and 10 mA (Brucker, Madison, WI, USA). The BET surface areas of the samples were analyzed by N$_2$ adsorption at −196 °C using a Micromeritics Tristar 3000 instrument (Micromeritics, Atlanta, GA, USA). X-ray photoelectron spectroscopy (XPS) measurements were performed on a Perkin–Elmer PHI 5000C spectrometer (Perkin-Elmer, Waltham, MA, USA). All binding energy values were calibrated using the C 1s peak at 284.6 eV. The surface basicity was measured by the temperature programmed desorption of CO$_2$ (CO$_2$-TPD) using a Micromeritics AutoChem II analyzer (Micromeritics, Atlanta, GA, USA); 0.2 g of sample was preheated at 750 °C for 1 h under He (30 mL/min), then cooled down to 80 °C. CO$_2$ adsorption was conducted at this temperature, followed by purging with He (30 mL/min) for 2 h. The temperature was then raised from 80 to 950 °C at a ramping rate of 10 °C/min. O$_2$ temperature programmed desorption (O$_2$-TPD) was performed on the same instrument; 0.2 g of sample was preheated at 750 °C for 1 h under He (30 mL/min), then cooled down to 50 °C. O$_2$ adsorption was conducted at this temperature, followed by purging with He (30 mL/min) for 2 h. The temperature was then raised from 50 to 800 °C at a ramping rate of 10 °C/min. The desorbed CO$_2$ and O$_2$ were detected with a thermal conductivity detector (TCD). Field-emission scanning electron microscopy (FESEM) images were taken using a Hitachi S-4800 instrument (Hitachi, Tokyo, Japan). Transmission electron microscopy (TEM) images were recorded on an FEI Tecnai G^2 F20 S-TWIN instrument (FEI, Hillsboro, OR, USA). Fourier transform infrared (FTIR) spectra were recorded on a Nicolet Avatar 360 spectrometer (Nicolet, Madison, WI, USA). 30 mg of the spent catalyst and 300 mg of KBr were first mixed uniformly; 40 mg of the mixture was then pressed into a self-supporting disk.

3.3. Catalytic Tests

The oxidative coupling of methane reaction was performed with a fixed-bed flow reactor at atmospheric pressure, with a quartz tube internal diameter of 6 mm. Here, 0.2 g of the catalyst (40–60 mesh) was placed in the middle of the reactor, with the downstream of the catalyst fixed with quartz wool. The catalytic performance was evaluated using a mixture of methane and oxygen (CH$_4$/O$_2$ = 4/1 molar ratio) as feed gas, with a total flow rate of 60 mL/min, which results in a gas hourly space velocity (GHSV) of 18,000 mL/(g•h). Before the reaction, the catalyst was pretreated at 750 °C in Ar (30 mL/min) for 1 h. The reaction temperature (actually the catalyst bed temperature) was monitored by a thermocouple placed in the middle of the catalyst bed. The reaction products were analyzed by an on-line GC equipped with a TCD and a 2-m Shincarbon ST packed column (for separation of H$_2$, O$_2$, CO, CH$_4$, and CO$_2$) and by another on-line GC equipped with a FID and a 50-m PoraPLOT Q capillary column (for the separation of CH$_4$, C$_2$H$_4$, C$_2$H$_6$, C$_3$H$_6$, and C$_3$H$_8$). Prior to the analysis using TCD, the products were passed through a cold trap at −3 °C to remove most of water generated during the reaction. The CH$_4$ conversion and C$_2$-C$_3$ selectivity were calculated using the standard normalization method based on carbon atom balance. The typical GC chromatograms showing the reaction products are given in Figure S4.

4. Conclusions

In this work, we developed Ho_2O_3 and Sr-Ho_2O_3 nanosheet catalysts for low-temperature OCM reaction. The HR-TEM images revealed that Ho_2O_3 and Sr-Ho_2O_3 nanosheets predominantly expose (222) facets. The Ho_2O_3 nanosheets outperformed Ho_2O_3 nanoparticles, which could be associated with the preferentially exposed (222) facet on the surface of the former catalyst. The ratio of $(O^- + O_2^-)/O^{2-}$, the amount of chemisorbed oxygen species, and the moderate basic sites were enhanced upon the addition of small amounts of Sr to Ho_2O_3 nanosheets, as demonstrated by XPS, O_2-TPD, and CO_2-TPD, respectively. This, in turn, resulted in an improved catalytic performance. The optimal $0.04Sr$-Ho_2O_3 nanosheets with a Sr/Ho molar ratio of 0.04 afforded a methane conversion of 24.0% with 56.7% C_2-C_3 selectivity at 650 °C. Moreover, this catalyst exhibited good stability in the OCM reaction for 60 h of time on stream. A good correlation between the C_2-C_3 yield and amount of moderate basic sites on the catalysts was established.

References

1.   Lee, J.; Oyama, S. Oxidative coupling of methane to higher hydrocarbons. *Catal. Rev. Sci. Eng.* **1988**, *30*, 249–280. [CrossRef]
2.   Arndt, S.; Laugel, G.; Levchenko, S.; Horn, R.; Baerns, M.; Scheffler, M.; Schlögl, R.; Schomäcker, R. A critical assessment of Li/MgO-based catalysts for the oxidative coupling of methane. *Catal. Rev. Sci. Eng.* **2011**, *53*, 424–514. [CrossRef]
3.   Han, B.; Yang, Y.; Xu, Y.; Etim, U.J.; Qiao, K.; Xu, B.; Yan, Z. A review of the direct oxidation of methane to methanol. *Chin. J. Catal.* **2016**, *37*, 1206–1215. [CrossRef]
4.   Mesters, C. A selection of recent advances in C1 chemistry. *Annu. Rev. Chem. Biomol. Eng.* **2016**, *7*, 223–238. [CrossRef] [PubMed]
5.   Galadima, A.; Muraza, O. Revisiting the oxidative coupling of methane to ethylene in the golden period of shale gas: A review. *J. Ind. Eng. Chem.* **2016**, *37*, 1–13. [CrossRef]
6.   Pierre, S.; Pan, X.L.; Bao, X.H. Direct conversion of methane to value-added chemicals over heterogeneous catalysts: Challenges and prospects. *Chem. Rev.* **2017**, *117*, 8497–8520.
7.   Gambo, Y.; Jalil, A.A.; Triwahyono, S.; Abdulrasheed, A.A. Recent advances and future prospect in catalysts for oxidative coupling of methane to ethylene: A review. *J. Ind. Eng. Chem.* **2018**, *59*, 218–229. [CrossRef]
8.   Keller, G.E.; Bhasin, M.M. Synthesis of ethylene via oxidative coupling of methane: I. Determination of active catalysts. *J. Catal.* **1982**, *73*, 9–19. [CrossRef]
9.   Ito, T.; Lunsford, J.H. Synthesis of ethylene and ethane by partial oxidation of methane over lithium-doped magnesium-oxide. *Nature* **1985**, *314*, 721–722. [CrossRef]
10.   Driscoll, D.J.; Martir, W.; Wang, J.X.; Lunsford, J.H. Formation of gas-phase methyl radicals over MgO. *J. Am. Chem. Soc.* **1985**, *107*, 58–63. [CrossRef]
11.   Peil, K.P.; Goodwin, J.G.; Marcelin, G. Surface phenomena during the oxidative coupling of methane over Li/MgO. *J. Catal.* **1991**, *131*, 143–155. [CrossRef]
12.   Nagaoka, K.; Karasuda, T.; Aika, K. The effect of SnO_2 addition to Li/MgO catalysts for the oxidative coupling of methane. *J. Catal.* **1999**, *181*, 160–164. [CrossRef]
13.   Amin, N.A.S.; Pheng, S.E. Influence of process variables and optimization of ethylene yield in oxidative coupling of methane over Li/MgO catalyst. *Chem. Eng. J.* **2006**, *116*, 187–195. [CrossRef]

14. Tang, L.; Yamaguchi, D.; Wong, L.; Burke, N.; Chiang, K. The promoting effect of ceria on Li/MgO catalysts for the oxidative coupling of methane. *Catal. Today* **2011**, *178*, 172–180. [CrossRef]

15. Arndt, S.; Simon, U.; Kiefer, K.; Otremba, T.; Siemensmeyer, K.; Wollgarten, M.; Berthold, A.; Schmidt, F.; Görke, O.; Schomäcker, R.; et al. Li/MgO catalysts doped with alio-valent ions. Part I: Structure, composition, and catalytic properties. *ChemCatChem* **2017**, *9*, 3583–3596. [CrossRef]

16. Fang, X.; Li, S.; Lin, J.; Gu, J.; Yan, D. Preparation and characterization of catalyst for oxidative coupling of methane. *J. Mol. Catal.* **1992**, *6*, 254–262.

17. Ji, S.; Xiao, T.; Li, S.; Chou, L.; Zhang, B.; Xu, C.; Hou, R.; York, A.P.E.; Green, M.L.H. Surface WO_4 tetrahedron: The essence of the oxidative coupling of methane over M-W-Mn/SiO_2 catalysts. *J. Catal.* **2003**, *220*, 47–56. [CrossRef]

18. Wang, J.; Chou, L.; Zhang, B.; Song, H.; Zhao, J.; Yang, J.; Li, S. Comparative study on oxidation of methane to ethane and ethylene over Na_2WO_4-Mn/SiO_2 catalysts prepared by different methods. *J. Mol. Catal. A* **2006**, *245*, 272–277. [CrossRef]

19. Arndt, S.; Otremba, T.; Simon, U.; Yildiz, M.; Schubert, H.; Schomäcker, R. Mn–Na_2WO_4/SiO_2 as catalyst for the oxidative coupling of methane. What is really known? *Appl. Catal. A* **2012**, *425–426*, 53–61. [CrossRef]

20. Ghose, R.; Hwang, H.T.; Varma, A. Oxidative coupling of methane using catalysts synthesized by solution combustion method: Catalyst optimization and kinetic studies. *Appl. Catal. A* **2014**, *472*, 39–46. [CrossRef]

21. Elkins, T.W.; Hagelin-Weaver, H.E. Characterization of Mn-Na_2WO_4/SiO_2 and Mn-Na_2WO_4/MgO catalysts for the oxidative coupling of methane. *Appl. Catal. A* **2015**, *497*, 96–106. [CrossRef]

22. Fleischer, V.; Steuer, R.; Parishan, S.; Schomäcker, R. Investigation of the surface reaction network of the oxidative coupling of methane over Na_2WO_4/Mn/SiO_2 catalyst by temperature programmed and dynamic experiments. *J. Catal.* **2016**, *341*, 91–103. [CrossRef]

23. Werny, M.J.; Wang, Y.; Girgsdies, F.; Schlögl, R.; Trunschke, A. Fluctuating storage of the active phase in a Mn-Na_2WO_4/SiO_2 catalyst for the oxidative coupling of methane. *Angew. Chem. Int. Ed.* **2020**, *59*, 14921–14926. [CrossRef]

24. Wang, P.; Zhao, G.; Wang, Y.; Lu, Y. $MnTiO_3$-driven low-temperature oxidative coupling of methane over TiO_2-doped Mn_2O_3-Na_2WO_4/SiO_2 catalyst. *Sci. Adv.* **2017**, *3*, e1603180. [CrossRef]

25. Huang, P.; Zhao, Y.; Zhang, J.; Zhu, Y.; Sun, Y. Exploiting shape effects of La_2O_3 nanocatalysts for oxidative coupling of methane reaction. *Nanoscale* **2013**, *5*, 10844–10848. [CrossRef]

26. Jiang, T.; Song, J.; Huo, M.; Yang, N.; Liu, J.; Zhang, J.; Sun, Y.; Zhu, Y. La_2O_3 catalysts with diverse spatial dimensionality for oxidative coupling of methane to produce ethylene and ethane. *RSC Adv.* **2016**, *6*, 34872–34876. [CrossRef]

27. Fu, B.; Jiang, T.; Zhu, Y. Structural effect of one-dimensional samarium oxide catalysts on oxidative coupling of methane. *J. Nanosci. Nanotechnol.* **2018**, *18*, 3398–3404. [CrossRef]

28. Fan, Y.; Sun, M.; Miao, C.; Yue, Y.; Hua, W.; Gao, Z. Morphology effects of nanoscale Er_2O_3 and Sr-Er_2O_3 catalysts for oxidative coupling of methane. *Catal. Lett.* **2021**, 1–10. [CrossRef]

29. Song, J.; Sun, Y.; Ba, R.; Huang, S.; Zhao, Y.; Zhang, J.; Sun, Y.; Zhu, Y. Monodisperse Sr–La_2O_3 hybrid nanofibers for oxidative coupling of methane to synthesize C_2 hydrocarbons. *Nanoscale* **2015**, *7*, 2260–2264. [CrossRef]

30. Sun, Y.; Shen, Y.; Song, J.; Ba, R.; Huang, S.; Zhao, Y.; Zhang, J.; Sun, Y.; Zhu, Y. Facet-controlled CeO_2 nanocrystals for oxidative coupling of methane. *J. Nanosci. Nanotechnol.* **2016**, *16*, 4692–4700. [CrossRef]

31. Wiktorczyk, T. Preparation and optical properties of holmium oxide thin films. *Thin Solid Films* **2002**, *405*, 238–242. [CrossRef]

32. Mortazavi-Derazkola, S.; Zinatloo-Ajabshir, S.; Salavati-Niasari, M. New facile preparation of Ho_2O_3 nanostructured material with improved photocatalytic performance. *J. Mater. Sci.* **2017**, *28*, 1914–1924. [CrossRef]

33. Zinatloo-Ajabshir, S.; Mortazavi-Derazkola, S.; Salavati-Niasari, M. Simple sonochemical synthesis of Ho_2O_3-SiO_2 nanocomposites as an effective photocatalyst for degradation and removal of organic contaminant. *Ultrason. Sonochem.* **2017**, *39*, 452–460. [CrossRef]

34. Shiri, H.M.; Ehsani, A. A novel and facile route for the electrosynthesis of Ho_2O_3 nanoparticles and its nanocomposite with p-type conductive polymer: Characterization and electrochemical performance. *Bull. Chem. Soc. Jpn.* **2016**, *89*, 1201–1206. [CrossRef]

35. Takenaka, S.; Kaburagi, T.; Yamanaka, I.; Otsuka, K. Oxidative coupling of methane over Li^+-added Y_2O_3 catalyst prepared from $Y(OH)_3$. *Catal Today* **2001**, *71*, 31–36. [CrossRef]

36. Campbell, K.D.; Morales, E.; Lunsford, J.H. Gas-phase coupling of methyl radicals during the catalytic partial oxidation of methane. *J. Am. Chem. Soc.* **1987**, *109*, 7900–7901. [CrossRef]

37. Al-Zahrani, S.; Song, Q.; Lobban, L.L. Effects of CO_2 during oxidative coupling of methane over Li/MgO: Mechanisms and models. *Ind. Eng. Chem. Res.* **1994**, *33*, 251–258. [CrossRef]

38. Vislovskii, V.P.; Baidikova, I.V.; Mamedov, E.A.; Rizayev, R.G. Promoting effect of alkali oxides on Bi-Mn catalysts activity in oxidative coupling of methane. *React. Kinet. Catal. Lett.* **1992**, *47*, 193–197. [CrossRef]

39. Baronetti, G.T.; Padró, C.; Scelza, O.A.; Castro, A.A. Structure and reactivity of alkali-doped calcium oxide catalysts for oxidative coupling of methane. *Appl. Catal. A* **1993**, *101*, 167–183. [CrossRef]

40. Zhao, M.; Ke, S.; Wu, H.; Xia, W.; Wan, H. Flower-like Sr-La_2O_3 microspheres with hierarchically porous structures for oxidative coupling of methane. *Ind. Eng. Chem. Res.* **2019**, *58*, 22847–22856. [CrossRef]

41. Kharas, K.C.C.; Lunsford, J.H. Catalytic partial oxidation of methane over barium metaplumbate $BaPbO_3$: Possible involvement of peroxide ion. *J. Am. Chem. Soc.* **1989**, *111*, 2336–2337. [CrossRef]

42. Peng, X.D.; Richards, D.A.; Stair, P.C. Surface composition and reactivity of lithium-doped magnesium oxide catalysts for oxidative coupling of methane. *J. Catal.* **1990**, *121*, 99–109. [CrossRef]

43. Ding, W.; Chen, Y.; Fu, X. Oxidative coupling of methane over Ce^{4+}-doped Ba_3WO_6 catalysts: Investigation on oxygen species responsible for catalytic performance. *Catal. Lett.* **1994**, *23*, 69–78. [CrossRef]

44. Hou, Y.H.; Han, W.C.; Xia, W.S.; Wan, H.L. Structure sensitivity of $La_2O_2CO_3$ catalysts in the oxidative coupling of methane. *ACS Catal.* **2015**, *5*, 1663–1674. [CrossRef]

45. Bai, Y.; Xia, W.; Weng, W.; Lian, M.; Zhao, M.; Wan, H. Influence of phosphate on La-based catalysts for oxidative coupling of methane. *Chem. J. Chin. Univ. Chin.* **2018**, *39*, 247–254.

46. Sayle, T.X.T.; Parker, S.C.; Sayle, D.C. Oxidising CO to CO_2 using ceria nanoparticles. *Phys. Chem. Chem. Phys.* **2005**, *7*, 2936–2941. [CrossRef]

47. Bernal, S.; Botana, F.J.; Garcia, R.; Rodriguez-Izquierdo, J.M. Behaviour of rare earth sesquioxides exposed to atmospheric carbon dioxide and water. *React. Soliak.* **1987**, *4*, 23–40. [CrossRef]

48. Djerdj, I.; Garnweitner, G.; Su, D.S.; Niederberger, M. Morphology-controlled nonaqueous synthesis of anisotropic lanthanum hydroxide nanoparticles. *J. Solid State Chem.* **2007**, *180*, 2154–2165. [CrossRef]

49. Farrukh, M.A.; Imran, F.; Ali, S.; Khaleeq-ur-Rahman, M.; Naqvi, I.I. Micelle assisted synthesis of La_2O_3 nanoparticles and their applications in photodegradation of bromophenol blue. *Russ. J. Appl. Chem.* **2015**, *88*, 1523–1527. [CrossRef]

50. Spinicci, R.; Tofanari, A. Characterization of catalysts for methane-coupling by means of temperature programmed desorption. *Catal. Today* **1990**, *6*, 473–479. [CrossRef]

51. Xu, J.; Zhang, Y.; Xu, X.; Fang, X.; Xi, R.; Liu, Y.; Zheng, R.; Wang, X. Constructing $La_2B_2O_7$ (B = Ti, Zr, Ce) compounds with three typical crystalline phases for the oxidative coupling of methane: The effect of phase structures, superoxide anions, and alkalinity on the reactivity. *ACS Catal.* **2019**, *9*, 4030–4045. [CrossRef]

52. McFarland, E.W.; Metiu, H. Catalysis by Doped Oxides. *Chem. Rev.* **2013**, *113*, 4391–4427. [CrossRef]

53. Liang, Q.; Wu, X.; Weng, D.; Xu, H. Oxygen activation on Cu/Mn−Ce mixed oxides and the role in diesel soot oxidation. *Catal. Today* **2008**, *139*, 113–118. [CrossRef]

54. Papa, F.; Luminita, P.; Osiceanu, P.; Birjega, R.; Akane, M.; Balint, I. Acid–base properties of the active sites responsible for C_2^+ and CO_2 formation over MO–Sm_2O_3 (M = Zn, Mg, Ca and Sr) mixed oxides in OCM reaction. *J. Mol. Catal. A* **2011**, *346*, 46–54. [CrossRef]

55. Elkins, T.W.; Roberts, S.J.; Hagelin-Weaver, H.E. Effects of alkali and alkaline-earth metal dopants on magnesium oxide supported rare-earth oxide catalysts in the oxidative coupling methane. *Appl. Catal. A* **2016**, *528*, 175–190. [CrossRef]

56. Bernal, S.; Blanco, G.; El Amarti, A.; Cifredo, G.; Fitian, L.; Galtayries, A.; Martín, J.; Pintado, J.M. Surface basicity of ceria-supported lanthana. Influence of the calcination temperature. *Surf. Interface Anal.* **2006**, *38*, 229–233. [CrossRef]

57. Peng, L.; Xu, J.; Fang, X.; Liu, W.; Xu, X.; Liu, L.; Li, Z.; Peng, H.; Zheng, R.; Wang, X. SnO_2 based catalysts with low-temperature performance for oxidative coupling of methane: Insight into the promotional effects of alkali-metal oxides. *Eur. J. Inorg. Chem.* **2018**, *2018*, 1787–1799. [CrossRef]

58. Xu, J.; Peng, L.; Fang, X.; Fu, Z.; Liu, W.; Xu, X.; Peng, H.; Zheng, R.; Wang, X. Developing reactive catalysts for low temperature oxidative coupling of methane: On the factors deciding the reaction performance of $Ln_2Ce_2O_7$ with different rare earth A sites. *Appl. Catal. A* **2018**, *552*, 117–128. [CrossRef]

59. Xu, J.; Zhang, Y.; Liu, Y.; Fang, X.; Xu, X.; Liu, W.; Zheng, R.; Wang, X. Optimizing the reaction performance of $La_2Ce_2O_7$-based catalysts for oxidative coupling of methane (OCM) at lower temperature by lattice doping with Ca cations. *Eur. J. Inorg. Chem.* **2019**, 183–194. [CrossRef]

60. Wang, Z.; Zou, G.; Luo, X.; Liu, H.; Gao, R.; Chou, L.; Wang, X. Oxidative coupling of methane over $BaCl_2$-TiO_2-SnO_2 catalyst. *J. Nat. Gas Chem.* **2012**, *21*, 49–55. [CrossRef]

61. Lee, H.I.; Lee, S.W.; Rhee, C.K.; Sohn, Y. Paramagnetic Ho_2O_3 nanowires, nano-square sheets, and nanoplates. *Ceram. Int.* **2018**, *44*, 17919–17924. [CrossRef]

62. Ito, T.; Wang, J.X.; Lin, C.H.; Lunsford, J.H. Oxidative dimerization of methane over a lithium-promoted magnesium oxide catalyst. *J. Am. Chem. Soc.* **1985**, *107*, 5062–5068. [CrossRef]